Surface electronic structure and evidence of plain *s*-wave superconductivity in $(Li_{0.8}Fe_{0.2})OHFeSe$

Y. J. Yan,[1] W. H. Zhang,[1] M. Q. Ren,[1] X. Liu,[1] X. F. Lu,[3] N. Z. Wang,[3] X. H. Niu,[1] Q. Fan,[1] J. Miao,[1] R. Tao,[1] B. P. Xie,[1,2] X. H. Chen,[3] T. Zhang,[1,2,*] and D. L. Feng[1,2,†]

[1]*State Key Laboratory of Surface Physics, Department of Physics, and Advanced Materials Laboratory, Fudan University, Shanghai 200433, China*

[2]*Collaborative Innovation Center of Advanced Microstructures, Fudan University, Shanghai 200433, China*

[3]*Hefei National Laboratory for Physical Science at Microscale and Department of Physics, University of Science and Technology of China, Hefei, Anhui 230026, People's Republic of China*

(Received 25 May 2016; revised manuscript received 11 September 2016; published 3 October 2016)

$(Li_{0.8}Fe_{0.2})OHFeSe$ is a newly discovered intercalated iron-selenide superconductor with a T_c above 40 K, which is much higher than the T_c of bulk FeSe (8 K). Here we report a systematic study of $(Li_{0.8}Fe_{0.2})OHFeSe$ by low temperature scanning tunneling microscopy (STM). We observed two kinds of surface terminations, namely FeSe and $(Li_{0.8}Fe_{0.2})OH$ surfaces. On the FeSe surface, the superconducting state is fully gapped with double coherence peaks, and a vortex core state with split peaks near E_F is observed. Through quasiparticle interference (QPI) measurements, we clearly observed intra- and interpocket scatterings in between the electron pockets at the M point, as well as some evidence of scattering that connects Γ and M points. Upon applying the magnetic field, the QPI intensity of all the scattering channels are found to behave similarly. Furthermore, we studied impurity effects on the superconductivity by investigating intentionally introduced impurities and intrinsic defects. We observed that magnetic impurities such as Cr adatoms can induce in-gap states and suppress superconductivity. However, nonmagnetic impurities such as Zn adatoms do not induce visible in-gap states. Meanwhile, we show that Zn adatoms can induce in-gap states in thick FeSe films, which is believed to have an $s_{\pm}$-wave pairing symmetry. Our experimental results suggest it is likely that $(Li_{0.8}Fe_{0.2})OHFeSe$ is a plain s-wave superconductor, whose order parameter has the same sign on all Fermi surface sections.

DOI: 10.1103/PhysRevB.94.134502

I. INTRODUCTION

The pairing mechanism is one of the pivotal issues in the study of iron-based superconductors [1,2]. Recently, heavily electron-doped iron selenide (HEDIS) superconductors, such as $A_xFe_{2-y}Se_2$ (A = K, Rb, Cs . . .) [3–5] and single-layer FeSe films on $SrTiO_3$ (STO) [6–11], have attracted tremendous interest. In these materials, the absence of holelike Fermi surfaces, together with the nodeless superconducting gap [5–9], greatly challenges existing theories, especially the weak coupling theories that were rather successful in predicting the $s_{\pm}$ pairing symmetry in iron pnictide superconductors [12,13]. Currently, there is no consensus regarding the pairing symmetry of HEDIS, and many forms of pairing symmetry have been proposed, including s_{++} wave, d wave, bonding-antibonding $s_{\pm}$ wave, etc. [13–18]. In the case of single layer FeSe/STO films, our recent scanning tunneling microscopy (STM) study showed that system to be a plain s-wave superconductor [19]. However, this may be a special case since signatures of strong interfacial electron-phonon interactions have been observed, which may play a dominant role in this interfacial superconducting system [10].

Recently, an intercalated FeSe-derived superconductor, $(Li_{0.8}Fe_{0.2})OHFeSe$, has been synthesized, which exhibits superconductivity above 40 K [20]. This material consists of alternating FeSe and $(Li_{0.8}Fe_{0.2})OH$ layers. Preliminary angle-resolved photoemission spectroscopy (ARPES) measurements indicated that it is also heavily electron doped with Fermi surfaces only at the M points, and there are no side bands induced by strong electron-phonon interactions, as observed in single layer FeSe/STO [21,22]. Because this material does not have intrinsic phase separation and is air stable, it is a promising candidate to study the superconductivity of HEDIS.

The STM is a powerful tool for studying superconductivity and gaining phase information of the order parameter [23–28]. In this paper, we report a systematic STM study on $(Li_{0.8}Fe_{0.2})OHFeSe$ single crystals. We observed two kinds of surface terminations on the cleaved sample, which we identified to be the FeSe and $(Li_{0.8}Fe_{0.2})OH$ surfaces. On the FeSe surface, we observed fully gapped tunneling spectra with double coherence peaks, which is similar to those of single-layer FeSe/STO [6]. Magnetic vortices were found to be spatially isotropic with double-peaked bound states at the core. On the $(Li_{0.8}Fe_{0.2})OH$ surface, a metallic state is observed without obvious superconducting gap opening. Quasiparticle interference (QPI) patterns on the FeSe surface revealed intra- and interpocket scattering of the electron pockets at M points. Meanwhile, a feature centered at $(\pi,0)$, which may correspond to Γ-M scattering, is observed near Fermi energy. To explore the pairing symmetry, we measured the magnetic field dependence of the QPI as well as the impurity effects on intentionally introduced impurities (deposited Cr and Zn atoms) and intrinsic defects. We found that (1) all the scattering channels in QPI behave similarly under magnetic field, including the feature at $(\pi,0)$, and (2) magnetic impurities such as Cr adatoms can induce in-gap states and locally suppress the superconductivity on FeSe surface, while the nonmagnetic Zn adatoms do not induce any visible in-gap states. Furthermore, we checked the effect of Zn atoms deposited on thick FeSe films (which is believed to have an

*tzhang18@fudan.edu.cn
†dlfeng@fudan.edu.cn

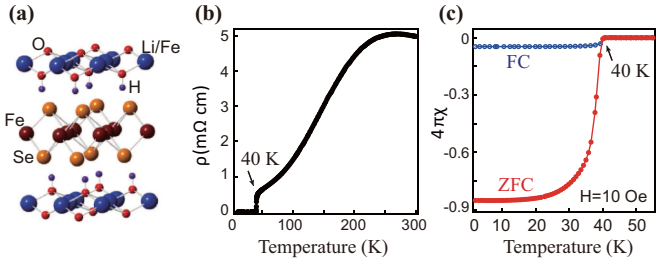

FIG. 1. (a) Schematic of the crystal structure of $(Li_{0.8}Fe_{0.2})$OHFeSe and (b) temperature dependence of the resistivity of the $(Li_{0.8}Fe_{0.2})$OHFeSe single crystal. (c) Temperature dependence of the dc magnetic susceptibility of $(Li_{0.8}Fe_{0.2})$OHFeSe measured through zero-field cooling (ZFC) and field cooling (FC).

$s_{\pm}$-wave symmetry [29,30]) and found that they *do* induce pronounced in-gap states in this case. We show that although a thorough understanding of the QPI and impurity effects will need more theoretical work when considering the microscopic details, our results do not show evidence of a sign change in $(Li_{0.8}Fe_{0.2})$OHFeSe. It is likely that $(Li_{0.8}Fe_{0.2})$OHFeSe is a plain s-wave superconductor whose order parameter has the same sign on all Fermi surface sections.

II. METHODS

The $(Li_{0.8}Fe_{0.2})$OHFeSe single crystals were grown by a novel hydrothermal method, as described in Ref. [20]. Temperature dependence of the electrical resistivity under zero magnetic field was measured by a standard dc four-probe method using a Quantum Design Physical Property Measurement System (PPMS). Temperature dependence of the magnetic susceptibility was measured using a Quantum Design Magnetic Property Measurement System (MPMS). The STM experiment was conducted in a cryogenic STM with a base temperature of 0.4 K. The sample was cleaved in a vacuum at 77 K and immediately transferred into the STM module. FeSe films (25 monolayers thick) were grown by co-deposition of high purity Se (99.999%) and Fe (99.995%) on graphitized SiC (0001) held at 620 K. The graphitized SiC (0001) substrates were prepared by direct heating of SiC (0001) at 1650 K. The STM measurements were taken at 4.2 K for $(Li_{0.8}Fe_{0.2})$OHFeSe and at 0.4 K for FeSe films. The Cr and Zn atoms were evaporated onto the surface at low temperatures (~50 K). The PtIr STM tips were used after being treated on a Au or Ag surface. The dI/dV spectroscopy was collected using a standard lock-in technique with modulation frequency $f = 973$ Hz and typical modulation amplitude (ΔV) 1 mV.

III. RESULTS AND DISCUSSION

A. Resistivity and magnetic susceptibility

Temperature dependence of the resistivity and dc magnetic susceptibility of $(Li_{0.8}Fe_{0.2})$OHFeSe single crystals has been measured, as shown in Fig. 1. A sharp superconducting transition at about 40 K is observed in Figs. 1(b) and 1(c), confirming the good quality of the $(Li_{0.8}Fe_{0.2})$OHFeSe crystal.

B. Surface topography and tunneling spectrum

As illustrated in Fig. 1(a), $(Li_{0.8}Fe_{0.2})$OHFeSe adopts a structure with alternate stacking of anti-PbO-type FeSe and $(Li_{0.8}Fe_{0.2})$OH layers, with an in-plane lattice constant of 3.78 Å [20]. The natural cleavage would expose either FeSe or $(Li_{0.8}Fe_{0.2})$OH terminated surfaces. In our STM study, indeed two kinds of surface terminations have been observed, as shown in Figs. 2(a) and 2(b). Judging from their topographic and spectroscopic characters (as shown throughout this paper), we attribute Fig. 2(a) as the FeSe-terminated surface and Fig. 2(b) as the $(Li_{0.8}Fe_{0.2})$OH-terminated surface. The FeSe surface is atomically flat with two kinds of intrinsic defects, as marked by I and II. Enlarged images of these are shown in Figs. 2(c) and 2(d), respectively. Type II defects are located at Se sites and are likely to be Se vacancies, as reported for thick FeSe films [29]. Type I defects are dimerlike, with the center located at the Fe site. They could be Fe vacancies [31] or substitutional impurities at the Fe site [32]. The $(Li_{0.8}Fe_{0.2})$OH surface is rougher than the FeSe surface, as shown in Fig. 2(b), probably due to the high level of Fe substitution for Li. Nevertheless, the atomic lattice can still be resolved [Fig. 2(b) inset] with a lattice constant the same as that of the FeSe surface. In addition, tunneling barrier heights were mapped to identify $(Li_{0.8}Fe_{0.2})$OH- and FeSe-terminated surfaces. The tunneling current I is expected to decay exponentially with the tip-sample distance z as $I \propto \exp(-Z\sqrt{8m\Phi/\hbar^2})$, where Φ is the local barrier height (LBH) that gives an estimation of work function. Averaged $I(z)$ curves measured on both surfaces with the same tip are shown in Fig. 2(e), which yields LBHs of 2.7 eV for the $(Li_{0.8}Fe_{0.2})$OH surface and 3.42 eV for the FeSe surface. This provides another way to distinguish these two surfaces.

Figure 2(f) displays typical dI/dV spectra taken on the two surface terminations. For the FeSe surface (red curve), a fully developed superconducting gap with double coherence peaks at ± 9 mV and ± 15 mV is observed. The gap bottom with nearly zero tunneling conduction is 5 meV wide. Note that both the gap structure and gap size are similar to that observed in single-layer FeSe/STO [6]. For the $(Li_{0.8}Fe_{0.2})$OH surface (blue curve), the spectrum shows metallic behavior with a weak dip at Fermi level. This indicates that the $(Li_{0.8}Fe_{0.2})$OH surface is metallic but likely *not* superconducting and implies that the coupling between FeSe and $(Li_{0.8}Fe_{0.2})$OH layers is rather weak.

C. Magnetic vortex

The superconductivity in the FeSe surface is further investigated by imaging magnetic vortices. Figure 3(a) shows a zero bias conductance (ZBC) mapping of a 50×50 nm^2 area, measured at $B = 11$ T. The vortices are clearly visible; however, the vortex lattice is highly disordered. By comparing with topography [see Fig. S1(a) in the Supplemental Material [33]], we found that this is because the dimerlike defects are strong pinning centers (they locally suppress superconductivity, as shown later). The pinned vortices (shown by yellow circles) have a different appearance than free vortices in the ZBC mapping, as highlighted in Fig. 3(a). For this reason, we studied only free vortices, as marked by white dashed circles. The

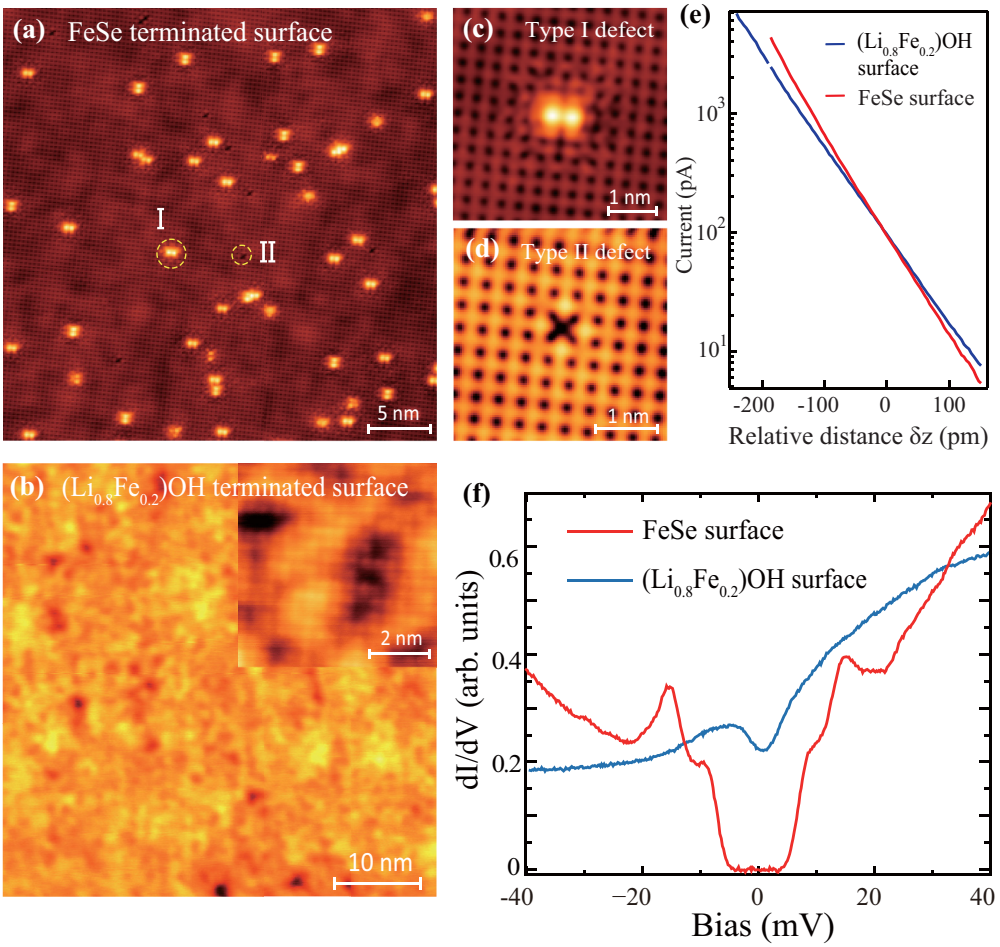

FIG. 2. Surface topography and dI/dV spectra of the $(Li_{0.8}Fe_{0.2})$OHFeSe single crystal. (a) Typical topographic image on the FeSe-terminated surface (bias voltage: $V_b = 50$ mV, current: $I = 10$ pA). Two types of defects (I, II) are marked, and expanded views of their morphologies are shown in (c) and (d). (b) Typical topographic image on the $(Li_{0.8}Fe_{0.2})$OH-terminated surface ($V_b = 100$ mV, $I = 50$ pA). Inset is the atomically resolved image ($V_b = 5$ mV, $I = 300$ pA). (e) The $I(z)$ curves measured on $(Li_{0.8}Fe_{0.2})$OH- and FeSe-terminated surfaces ($V_b = 200$ mV, $I = 100$ pA). (f) Averaged superconducting gap spectra on FeSe- and $(Li_{0.8}Fe_{0.2})$OH-terminated surfaces ($V_b = 40$ mV, $I = 150$ pA, $\Delta V = 1$ mV).

overall shape of a single free vortex is spatially isotropic [see Fig. 3(b) inset], which differs from the elongated vortices in FeSe thick films [29]. An exponential fit to the line profile of the Fig. 3(b) inset gives an estimate for the Ginzburg-Landau coherence length (ξ) of 2.3 nm.

Figure 3(c) shows the spectrum taken at the center of a free vortex core (red curve): A pair of peaks at energies of ± 2.1 meV with asymmetric intensities is observed. Away from the core center, these two peaks shift to higher energy and eventually merge into the gap edge [Fig. 3(d), shown in false color], and the double-gap structure is recovered [blue curve in Fig. 3(c)]. The presence of the core state with a pair of peaks is consistent with fully gapped superconductivity and indicates that the system is in the quantum limit [34–36], where the thermal smearing is sufficiently low that one can resolve the bound states having energies $E_p = \pm\Delta^2/2E_b$ (E_b is the occupied band width; see more discussion in the Supplemental Material, part I [33]). By using the larger gap value of $\Delta = 15$ meV and $E_p = 2.1$ meV, we get $E_b = 53$ meV. This agrees well with the occupied width of the electron bands at M, measured by ARPES [21,22] and our QPI data shown below.

D. Electronic structure

To further examine the electronic structure of $(Li_{0.8}Fe_{0.2})$OHFeSe, we performed dI/dV mappings to reveal the QPI patterns. A set of dI/dV maps was made within the energy range of ± 30 meV for a 35×35 nm^2 area on the FeSe surface; several of the maps are in Figs. 4(a)–4(h) and clearly show interference modulation around defects. (The mapping area is the same as that shown in Fig. 2(a); see also Fig. S2 in the Supplemental Material [33] for a complete set of dI/dV maps.) Figure 4(i) shows the comparison of the QPI intensities at $V_b = 6$ meV and -6 meV along the same line cut crossing the same defect. The antiphase relation of the QPI modulation near the defect can be seen, which is a characteristic of Bogoliubov quasiparticles.

Figures 5(a)–5(h) show the fast Fourier transforms (FFT) of the dI/dV maps in Figs. 4(a)–4(h). The FFTs are fourfold symmetrized to reduce noise since all of the QPI patterns were found to be fourfold symmetric (see also Fig. S2 in the Supplemental Material [33] for the raw FFTs). The common features throughout Figs. 5(a)–5(h) are ringlike

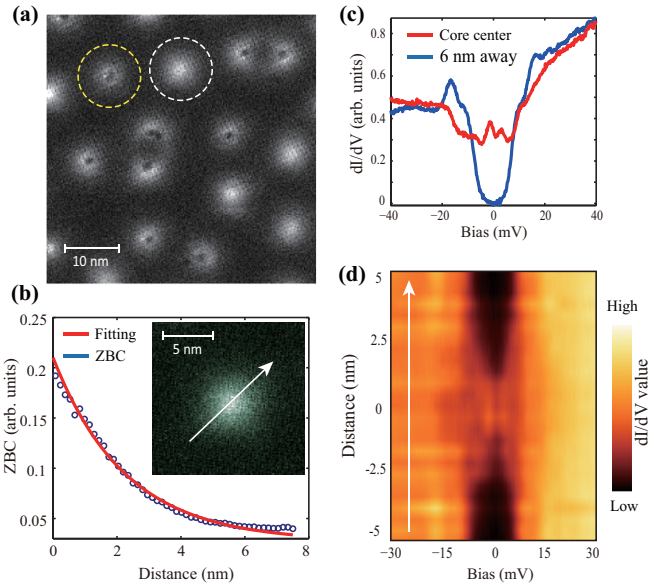

FIG. 3. Vortex mapping on the FeSe-terminated surface. (a) Vortex mapping on the FeSe-terminated surface at $V_b = 0$ mV under 11 T magnetic field. The vortex in the yellow circle with suppressed intensity near the core center is pinned by the dimerlike defects, while the vortex in the white circle is a free vortex that is not pinned. (b) Exponential fit to the line profile of a single free vortex in the ZBC mapping. Inset: a zoomed-in ZBC map of a single free vortex. (c) The dI/dV spectra taken at the vortex core center and 6 nm away from the center ($V_b = 40$ mV, $I = 100$ pA, $\Delta V = 1$ mV). (d) Evolution of the dI/dV spectra taken along the line across the free vortex core, as marked in the inset of (b), shown in false color.

patterns centered at (0, 0), (π,π), and $(0,2\pi)$ (marked as Ring 1, Ring 2, and Ring 3, respectively), which have also been observed in single-layer FeSe/STO [19,37]. These features originate from intra- and interpocket scattering of the electron pockets at the M points of the Brillouin Zone (BZ), as sketched in Fig. 5(i). In Fig. 5(j), we show the simulated FFT from calculating the joint density of states (JDOS), based on the *unfolded* Fermi surface shown in Fig. 5(i) (solid curves). One found that the ringlike features are well reproduced in the simulation, while the fourfold anisotropy of Ring 1 and the oval shape of Ring 3 [as clearly seen in Figs. 5(b)–5(d)] can also be reproduced by considering finite ellipticity of the electron pockets. Fitting to Ring 3 in Fig. 5(b) yields an ellipse with a long to short axis ratio of 1.1. We found that the unfolded Fermi surface can actually produce better FFT simulation than the folded Fermi surface, which likely means the BZ folding effect is *weak* in this system (see Fig. S4 in the Supplemental Material [33] for more details). According to the simulation, the radius of Ring 2 is twice the average radius of the electron pockets. In Fig. 5(k), we show the azimuth-averaged FFT line cuts surrounding (π,π) [as marked in Fig. 5(b)], taken at various energies outside the gapped region. The dispersion of Ring 2 is clearly seen, and parabolic fitting yields a band bottom at -50 (± 5) meV and an averaged Fermi crossing (k_F) of 0.21 (± 0.1) Å^{-1}. These agree well with the ARPES measurements [21,22] and are close to the values of single-layer FeSe/STO [7–9] (band bottom at -60 meV and $k_F = 0.22$ Å^{-1}). One may notice that Ring 2 appears to split into two rings at $E < -10$ meV [see Figs. 5(h), 5(k), and Fig. S2 in the Supplemental Material [33]]. The inner ring follows the parabolic dispersion, but the outer ring is almost nondispersive. The origin of this splitting is unclear and needs further investigation.

Interestingly, besides the ringlike structures, there are other features in the QPI on the FeSe surface. From Figs. 5(c)–5(h) and the FFT line cuts summarized in Fig. 5(l), one sees that below $E = 20$ meV, some features appear around $(\pi,0)$ with increasing intensity as the energy decreases. It is clearly separated from other scattering channels and persists across E_F. As sketched in Fig. 5(i), the position of this scattering corresponds to q_4, which connects the Γ and M points. Since this feature disappears above 20 meV and becomes pronounced at low energies, it likely arises from scattering between the holelike pocket at Γ and the electron pocket at M. However, ARPES data on $(Li_{0.8}Fe_{0.2})$OHFeSe indicates that the top of the hole band at Γ is 50 meV below E_F and that there are no other bands crossing E_F around Γ [21,22]. Thus, the origin of this possible Γ-M scattering is puzzling. One may speculate that the hole band at Γ may still have some residual weight near E_F, which could be due to the broadening of impurity scattering. We noticed that some theoretical works suggest that such a band without clear Fermi level crossing (incipient band) may still play an important role on superconductivity [38,39].

The QPI measurements on $(Li_{0.8}Fe_{0.2})$OH surfaces were also performed. Figures 6(a)–6(d) are selected dI/dV maps in a 120×120 nm^2 area, and the corresponding FFT images are shown in Figs. 6(e)–6(h) (see Fig. S3 in the Supplemental Material [33] for a complete set of dI/dV maps and FFTs). A single, circular scattering ring is observed around (0, 0), without any other high-q features. Meanwhile, the size of the ring decreases with decreasing energy, indicating that it is likely from the intraband scattering of a two-dimensional (2D) electron pocket. In Fig. 6(g), we summarize that the FFT line cuts though the center of the scattering ring. A parabolic fit to the dispersion yields a band bottom at -50 meV and a Fermi crossing at 0.09 Å^{-1}. Since the $(Li_{0.8}Fe_{0.2})$OH layers act as an electron reservoir that provides electrons to the FeSe layers, the existence of an electron pocket on this surface could be expected. We note that such a Fermi pocket is not observed in the ARPES studies, which may be due to the negligible photoemission matrix element of these states [21,22].

So far our measurement confirms well-developed superconductivity at the FeSe surface. It is expected that the FeSe layer may lose half of its bulk electron carriers after cleavage; however, the similar observed band structure to that of single-layer FeSe/STO and the well-developed superconducting gap indicate that the exposed FeSe layer is still sufficiently doped. The absence of a superconducting gap on the $(Li_{0.8}Fe_{0.2})$OH surface indicates weak coupling between the $(Li_{0.8}Fe_{0.2})$OH and neighboring FeSe layers. Thus the FeSe-terminated surface structurally resembles single-layer FeSe/STO except that the STO substrate is now replaced by the $(Li_{0.8}Fe_{0.2})$OH layer, which decouples the top FeSe layer from the bulk. The feature observed here apart from the single-layer FeSe/STO is the possible Γ-M scattering at $(\pi,0)$.

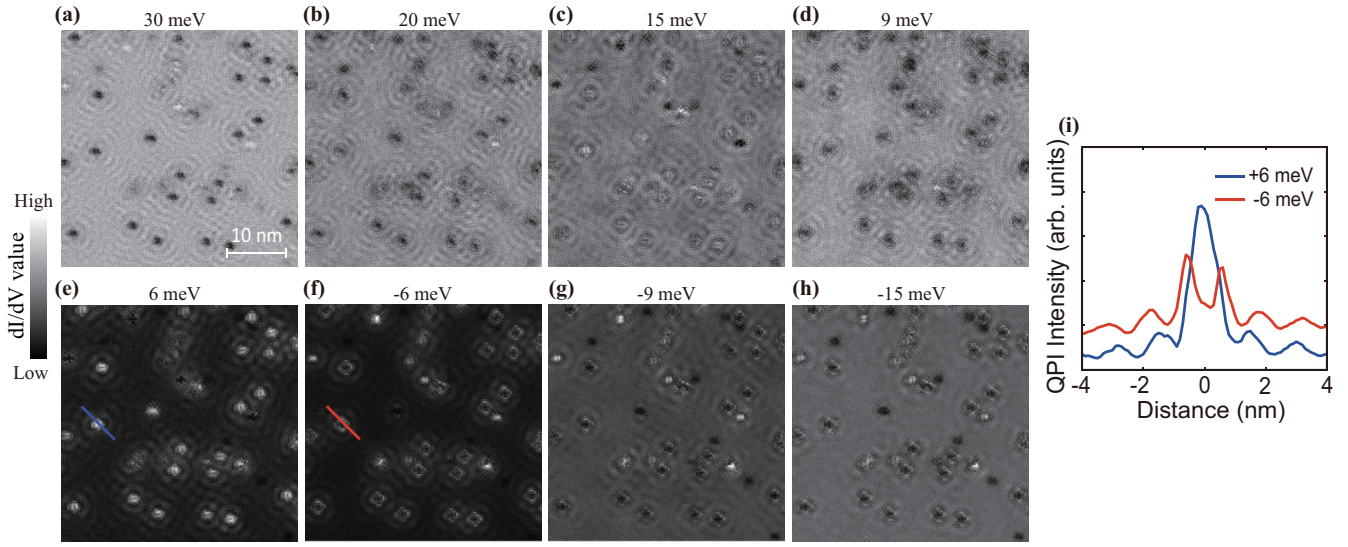

FIG. 4. (a)–(h) The dI/dV maps on the FeSe-terminated surface taken at different bias voltage, in the same $35 \times 35\,\mathrm{nm}^2$ area. Set point: $V_b = 30\,\mathrm{mV}$, $I = 150\,\mathrm{pA}$. (i) Line cut profiles taken along the line shown in (e) and (f).

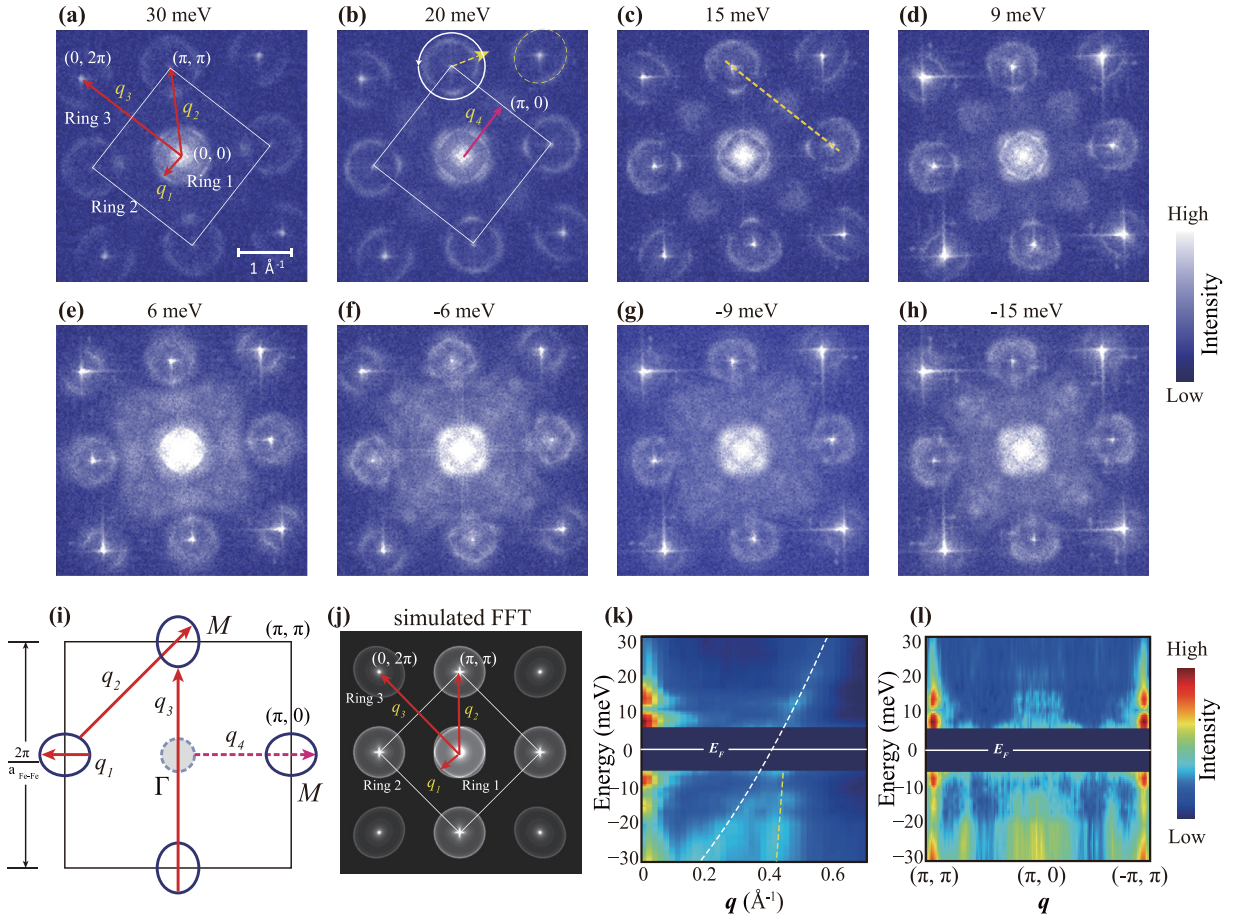

FIG. 5. The QPI patterns on FeSe-terminated surfaces. (a)–(h) The FFT transformations of the dI/dV maps shown in Figs. 4(a)–4(h). The white square represents the unfolded Brillouin zone. Different scattering channels are indicated by the red arrows. (i) Schematic of the unfolded Brillouin zone and Fermi surface of the FeSe surface. The dashed circle indicates the possible residual weight of holelike pocket at Γ. The possible scattering channels are marked by $q_1 \sim q_4$. (j) Simulated FFT corresponding to the Fermi surface shown in (i) (without the pocket at the Γ point). (k) The FFT line cuts extracted from the yellow dashed arrow in (b) and azimuth averaged with respect to (π,π), taken at various V_b and shown in false color. The white dashed curve is a parabolic fit to the dispersion of Ring 2. The yellow dashed curve indicates the splitting of Ring 2 below $-10\,\mathrm{meV}$. (l) The FFT line cuts extracted along the yellow dashed line in (c), taken at various V_b and shown in false color.

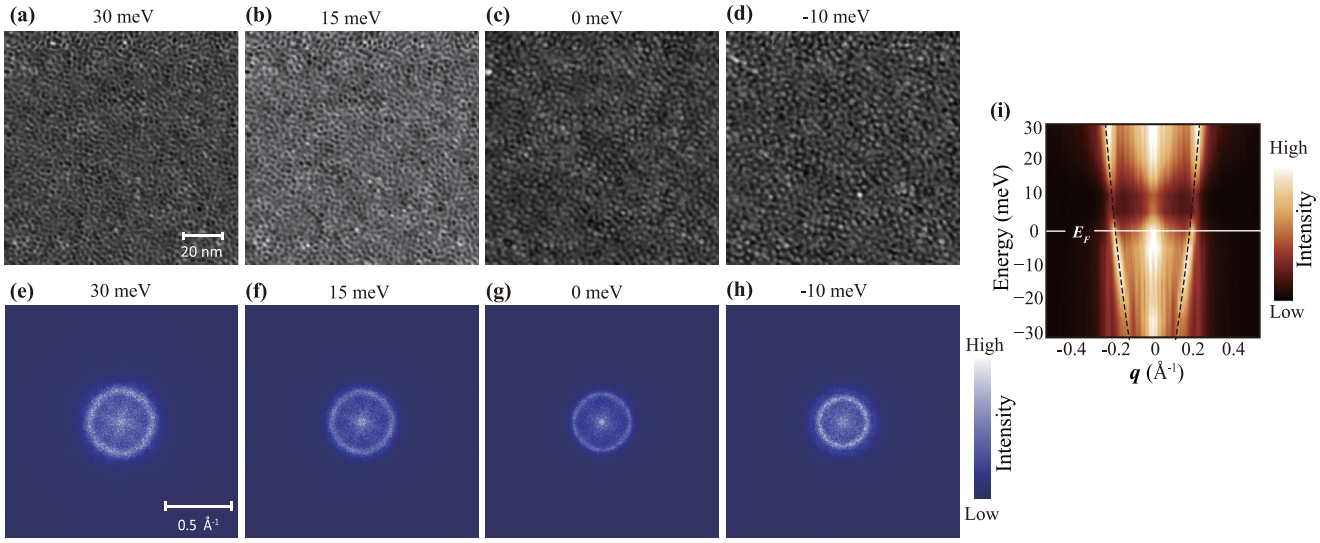

FIG. 6. The QPI patterns on $(Li_{0.8}Fe_{0.2})$OH-terminated surfaces. (a)–(d) The dI/dV maps taken in a $120 \times 120\,nm^2$ area of the $(Li_{0.8}Fe_{0.2})$OH-terminated surface. The mapping energies are labeled in the images. Each map has 400×400 pixels. (e)–(h) The FFTs of the dI/dV maps shown in panels (a)–(d) (fourfold symmetrized). (i) Line cuts extracted from the FFTs of the $(Li_{0.8}Fe_{0.2})$OH surface at various V_b, shown in false color. The black dashed curve is a parabolic fit to the dispersion of the scattering ring, which indicates an electron pocket.

As theoretically predicted, such a scattering channel may lead to a sign-changing $s_{\pm}$-wave pairing (even the Γ band does not have a Fermi surface) [12,13,39]. Thus, it would be important to check the pairing symmetry of this system.

E. Magnetic field dependent QPI

In the STM study, one way to gain phase information of superconducting order parameter (Δ_k) is to check the magnetic field dependence of the QPI. In a previous study of cuprate [25], it is found that in the presence of magnetic vortices, the scatterings that preserve the sign of Δ_k were enhanced, and the scatterings that change the sign of Δ_k were suppressed. Similar effect has also been observed in $FeTe_xSe_{1-x}$, which is believed to have an $s_{\pm}$-wave pairing [30]. Further theoretical works show that the disordered vortex cores, which locally suppressed the order parameter [40,42], and/or the impurities inside the vortex core, which acquire additional resonant or Andreev scattering [41], can indeed enhance the sign-preserving scattering channel. Meanwhile, the strength of sign-changing scattering is likely not directly affected by vortices; a weak, overall suppression of all of the scatterings may be expected due to the additional phases acquired by quasiparticles moving through disordered vortex lattice [30,40]. Therefore, one may still expect that the sign-changing and sign-preserving scatterings will show different intensity change under the magnetic field. In our case, the observed vortex lattice [Fig. 3(a)] is significantly disordered, and a part of the vortices are pinned around defects, which satisfies the condition discussed in Refs. [40–42].

We then carried out dI/dV mapping under magnetic fields of 0 T and 11 T in the same scan area ($32 \times 32\,nm^2$) within the energy range of ± 30 meV. Figures 7(a)–7(d) show dI/dV maps and their FFTs taken at $V_b = 12$ meV under $B = 0$ T and 11 T for comparison (see Fig. S5 in the Supplemental Material [33] for comparisons at more energies). In Fig. 7(e), we show the difference of the QPI intensities between Figs. 7(c) and 7(d). Here we intentionally suppressed the intensity near (0, 0) and all the Bragg spots because they are either irrelevant to QPI or could introduce artifacts. One sees that apparently an overall suppression occurs for all scattering channels. We then compare the relative change of the intensities of different scattering channels as a function of energy. The scattering intensities of each channel are obtained through integrating relevant areas in the FFT maps [shaded areas in Fig. 7(c)], again excluding the regions near (0, 0) and the Bragg spots. As shown in Fig. 7(f), all the scattering channels show similar suppression in the amplitude when the energy approaches the gap edge, including the possible Γ-M scattering (q_4). Thus, despite the fact that the overall suppression requires further quantitative explanation, no evidence is observed as an indication of sign-changing scatterings here.

F. Impurity effect

Besides the QPI measurement, impurity-induced effects are another way to explore the pairing symmetry. In general, the response of superconductivity to local impurities depends on the pairing symmetry and the characteristic of the impurities [26]. It is known that for s-wave pairing, only magnetic impurities can break the Cooper pair and induce in-gap bound states [43]. However, for phase-changing pairing symmetries such as d wave and $s_{\pm}$ wave, it is predicted that nonmagnetic impurities with proper scattering potentials can also induce in-gap states and suppress superconductivity [44–46], which is supported by STM measurements on cuprates [28], NaFeAs [32], and LiFeAs [47]. Meanwhile, several theoretical works have shown that nonmagnetic impurities can also help to identify the pairing symmetry of $K_xFe_{2-y}Se_2$ [48–50], which has a similar band structure as $(Li_{0.8}Fe_{0.2})$OHFeSe.

We investigated the impurity effect in $(Li_{0.8}Fe_{0.2})$OHFeSe, by controllably introducing impurities on the FeSe surface, as well as by studying the intrinsic defects. In the first case, impurity atoms Cr (magnetic) and Zn (nonmagnetic) were

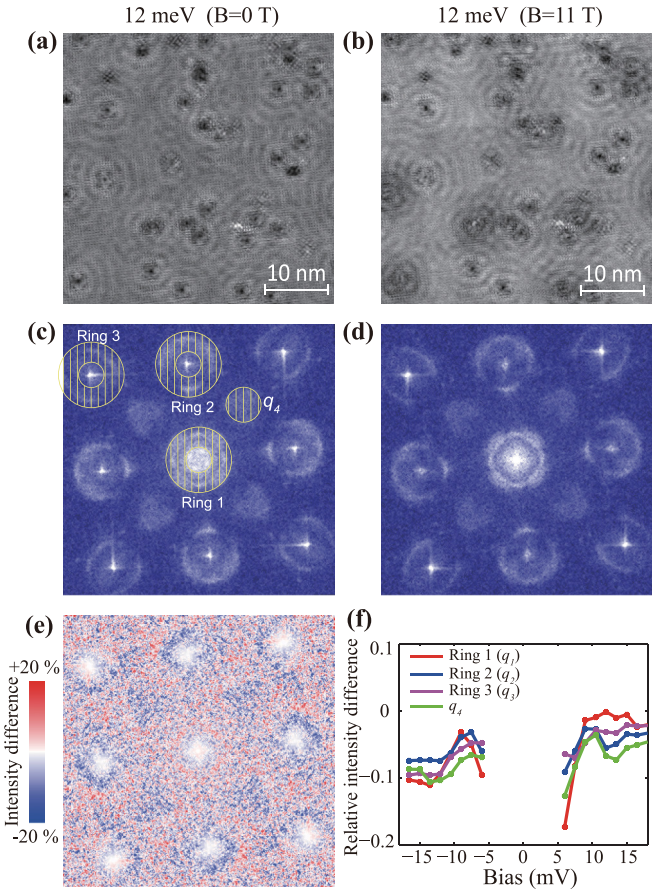

FIG. 7. Magnetic field dependence of QPI patterns on FeSe-terminated surface. (a) and (b) The dI/dV maps taken under magnetic fields of 0 T and 11 T in the same scan area at $V_b = 12$ mV. Set point: $V_b = 30$ mV, $I = 150$ pA. (c) and (d) The FFTs of the dI/dV maps shown in (a) and (b), respectively. Masked areas in (c) show the integration windows for different scattering channels. (e) The difference in QPI intensities at $V_b = 12$ mV, which is calculated by $(\mathrm{FFT}_{11\mathrm{T}} - \mathrm{FFT}_{0\mathrm{T}})/(\mathrm{FFT}_{11\mathrm{T}} + \mathrm{FFT}_{0\mathrm{T}})$. The $\mathrm{FFT}_{11\mathrm{T}}$ and the $\mathrm{FFT}_{0\mathrm{T}}$ are shown in (d) and (c), respectively. The intensity near (0, 0) and all Bragg spots are suppressed by a factor of $1-\Sigma[\mathrm{Gaussian}(q_{(\mathrm{Bragg})},\sigma)]$. All scattering channels are suppressed under high magnetic field. (f) The relative change of the intensities of different scattering channels, as a function of energy. The scattering intensities of each channel were obtained through integrating the relevant area in the FFT maps, as shown in (c).

deposited separately onto the sample holding at low temperature (~50 K). These atoms appear as bright protrusions on the FeSe surface in the topography [Figs. 8(a) and 8(b)]. Assuming the interaction between the low-temperature adsorbed atoms and underlying FeSe lattice to be weak, the impurity atoms are expected to retain their magnetic/nonmagnetic character after adsorption. In Figs. 8(c) and 8(d), we show local tunneling spectra near Cr and Zn atoms. On the Cr site, the superconducting gap is greatly suppressed, and a pair of asymmetric peaks appear in the gap. These are hallmarks of impurity-induced in-gap states. Away from the Cr site, the impurity states are weakened, and the superconducting gap gradually recovers. Meanwhile, for a Zn impurity, the superconducting gap size remains unchanged at and near the Zn site. Although the

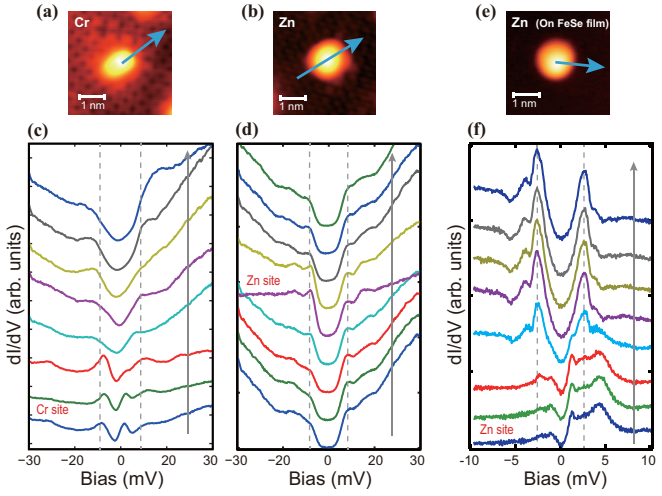

FIG. 8. Impurity-induced effects on the superconductivity of $(Li_{0.8}Fe_{0.2})$OHFeSe and thick FeSe films. (a) and (b) Topographic images of single Cr and Zn adatoms on the FeSe-terminated surface of $(Li_{0.8}Fe_{0.2})$OHFeSe. (c) and (d) Series of dI/dV spectra taken along the arrows shown in (a) and (b), respectively. The gray dashed lines indicate the position of the coherence peak at ± 9 meV for $(Li_{0.8}Fe_{0.2})$OHFeSe. (e) Topographic image of a single Zn adatom on a thick FeSe film. (f) Series of dI/dV spectra taken along the arrow (e). The gray dashed lines indicate the position of the coherence peaks at ± 2.5 meV for FeSe films.

coherence peaks at ± 9 meV change in intensity near Zn sites, there is no evidence of in-gap states.

The absence of in-gap states at nonmagnetic impurities intuitively suggests an s-wave pairing without sign change. However, because Fe-based superconductors are multiband systems, recent theoretical works show that the formation of sharp in-gap states on nonmagnetic impurities is not only subject to pairing symmetry but also highly depends on the details of band structure and the strength of scattering potentials [51]. Here we are not going to give a theoretical calculation considering all the details of $(Li_{0.8}Fe_{0.2})$OHFeSe band structure and the scattering potentials of Zn adatoms, which could be difficult to determine. Instead we performed a comparison experiment—checking the impurity effect of a Zn adatom on undoped FeSe, which is widely believed to have an $s_{\pm}$-wave pairing [29]. We grew 25 ML thick FeSe film on SiC substrate (see the Methods section), and Zn atoms were deposited on such film the same way as for $(Li_{0.8}Fe_{0.2})$OHFeSe. Figures 8(e) and 8(f) show the topography and local tunneling spectra near a Zn adatom on thick FeSe films, respectively. One can clearly see that at the Zn site, the superconducting gap of undoped FeSe film is dramatically suppressed, and a pair of in-gap states emerge at ± 1.2 meV. The presence of in-gap states strongly supports the phase-changing pairing in undoped FeSe and indicates that Zn adatoms are effective scatterers for this multiband system. The remarkable different response of $(Li_{0.8}Fe_{0.2})$OHFeSe to the same Zn impurity could arise from the pairing symmetry as well as its different electron structure to undoped FeSe.

We also measured the impurity effects induced by intrinsic defects (Fig. 9). Figure 9(c) shows the tunneling spectra taken

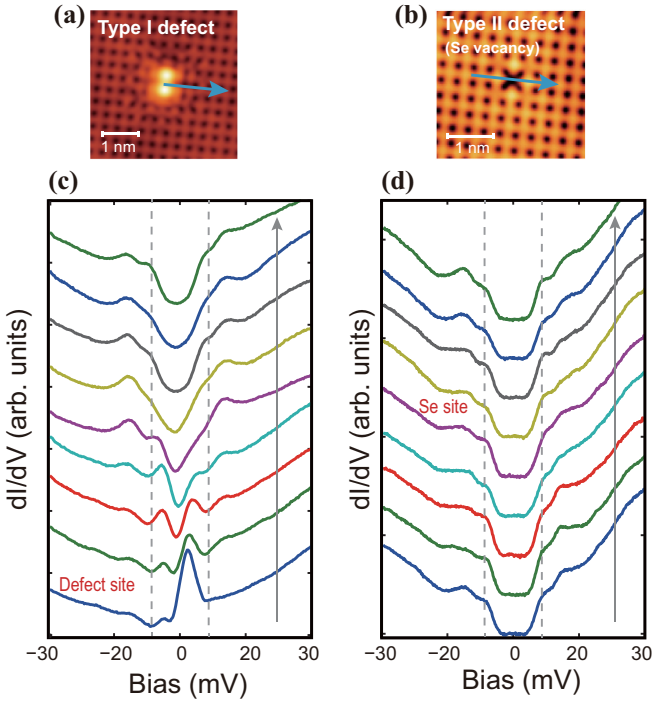

FIG. 9. Intrinsic-defect-induced effects on the superconductivity of $(Li_{0.8}Fe_{0.2})$OHFeSe. (a) and (b) Topographic images of type I defect (dimerlike defect on Fe site) and type II defect (Se vacancy) on an FeSe-terminated surface of $(Li_{0.8}Fe_{0.2})$OHFeSe. (c) and (d) Series of dI/dV spectra taken along the arrows, shown in (a) and (b), respectively. The gray dashed lines indicate the position of the coherence peaks at ± 9 meV.

near a dimerlike type I defect in Fig. 9(a). At the center of the dimer, in-gap states with asymmetric intensities at ± 3 meV are observed, and the superconducting gap is almost completely suppressed. Since the type I defects should be Fe vacancies or substitutional impurities on the Fe site, they are likely to carry spin and to be magnetic. We note that in $K_xFe_{2-y}Se_2$, Fe vacancies have been experimentally proven to be magnetic and to induce in-gap states [31]. The strong local suppression of superconductivity makes type I defects effective pinning sites for magnetic vortices. Tunneling spectra for type II defects, which we attribute to Se vacancies, are shown in Fig. 9(d). In contrast to type I defects, the superconducting gap is unaffected at the defect (Se) site; nearby, no in-gap states are observed. We noticed that Se vacancies in thick FeSe films *do* induce in-gap states and suppress superconductivity, as reported previously in Ref. [29]. Thus, it gives another instance in which the same type of impurity can have different effects in undoped FeSe and $(Li_{0.8}Fe_{0.2})$OHFeSe. One may speculate that the Se vacancies are nonmagnetic, which play a similar role as Zn adatoms. Overall, the impurity effects we observed are consistent in that only magnetic impurities induce in-gap states in $(Li_{0.8}Fe_{0.2})$OHFeSe, while nonmagnetic ones do not.

Upon finishing this paper, we noticed a theoretical work that shows that nonmagnetic impurities may not induce observable in-gap states for incipient $s_{\pm}$-wave pairing [52]. In this scenario, the gap changes sign on the incipient hole band, which does *not* have a Fermi surface. Identification of such a sign change may require more phase sensitive methods beyond the impurity effect. Also noted upon finishing this paper was another independent STM study on $(Li_{0.8}Fe_{0.2})$OHFeSe in Ref. [54].

IV. CONCLUSION

Overall, our STM study revealed distinct electron structure on FeSe and $(Li_{0.8}Fe_{0.2})$OH terminated surface of $(Li_{0.8}Fe_{0.2})$OHFeSe and offers several independent hints for the pairing symmetry. Fully gapped tunneling spectra and double-peaked vortex core states indicate a nodeless superconducting state. Magnetic field dependence of QPI and impurity effects did not show a sign of phase change, although some evidence of Γ-M scattering is observed. Magnetic impurities can induce in-gap states, but nonmagnetic ones, such as Zn adatoms, do not. These results together would suggest a plain s-wave pairing in $(Li_{0.8}Fe_{0.2})$OHFeSe, whose order parameter has the same sign on all Fermi surface sections. Previously, we have shown that single-layer FeSe/STO is also a plain s-wave superconductor, where side bands due to strong interfacial electron-phonon interactions were observed [10], while the side bands are absent in the ARPES data of $(Li_{0.8}Fe_{0.2})$OHFeSe [22]. All these findings show that the s_{++} pairing symmetry is likely a robust feature of HEDIS. This finding is consistent with strong-coupling theories based on local antiferromagnetic coupling [14,17] or orbital-fluctuation-mediated pairing mechanism [53].

ACKNOWLEDGMENTS

We thank professors J. P. Hu, Y. Chen, and Dr. Y. W. Guo for helpful discussions. This work is supported in part by the National Science Foundation of China (China), National Key R&D Program of the MOST of China (Grant No. 2016YFA0300200), Science Challenge Program of China, and Shanghai Rising-Star Program (A type) of Shanghai Science and Technology Committee (China).

[1] Y. Kamihara, T. Watanabe, M. Hirano, and H. Hosono, J. Am. Chem. Soc. **130**, 3296 (2008).
[2] F. C. Hsu, J. Y. Luo, K. W. Yeh, T. K. Chen, T. W. Huang, P. M. Wu, Y. C. Lee, Y. L. Huang, Y. Y. Chu, D. C. Yan, and M. K. Wu, Proc. Natl. Acad. Sci. USA **105**, 14262 (2008).
[3] J. G. Guo, S. F. Jin, G. Wang, S. C. Wang, K. X. Zhu, T. T. Zhou, M. He, and X. L. Chen, Phys. Rev. B **82**, 180520 (2010).
[4] A. F. Wang, J. J. Ying, Y. J. Yan, R. H. Liu, X. G. Luo, Z. Y. Li, X. F. Wang, M. Zhang, G. J. Ye, P. Cheng, Z. J. Xiang, and X. H. Chen, Phys. Rev. B **83**, 060512 (2011).
[5] Y. Zhang, L. X. Yang, M. Xu, Z. R. Ye, F. Chen, C. He, H. C. Xu, J. Jiang, B. P. Xie, J. J. Ying, X. F. Wang, X. H. Chen, J. P. Hu, M. Matsunami, S. Kimura, and D. L. Feng, Nat. Mater. **10**, 273 (2011).
[6] Q. Y. Wang, Z. Li, W. H. Zhang, Z. C. Zhang, J. S. Zhang, W. Li, H. Ding, Y. B. Ou, P. Deng, K. Chang, J. Wen, C. L. Song, K. He, J. F. Jia, S. H. Ji, Y. Y. Wang, L. L. Wang, X. Chen, X. C. Ma, and Q. K. Xue, Chin. Phys. Lett. **29**, 037402 (2012).
[7] D. F. Liu, W. H. Zhang, D. X. Mou, J. F. He, Y. B. Ou, Q. Y. Wang, Z. Li, L. L. Wang, L. Zhao, S. L. He, Y. Y. Peng, X. Liu,

C. Y. Chen, L. Yu, G. D. Liu, X. L. Dong, J. Zhang, C. T. Chen, Z. Y. Xu, J. P. Hu *et al.*, Nat. Commun. **3**, 931 (2012).
[8] S. L. He, J. F. He, W. H. Zhang, L. Zhao, D. F. Liu, X. Liu, D. X. Mou, Y. B. Ou, Q. Y. Wang, Z. Li, L. L. Wang, Y. Peng, Y. Liu, C. Chen, L. Yu, G. Liu, X. L. Dong, J. Zhang, C. T. Chen, Z. Y. Xu *et al.*, Nat. Mater. **12**, 605 (2013).
[9] S. Y. Tan, Y. Zhang, M. Xia, Z. Y. Ye, F. Chen, X. Xie, R. Peng, D. F. Xu, Q. Fan, H. C. Xu, J. Jiang, T. Zhang, X. C Lai, T. Xiang, J. P Hu, B. P Xie, and D. L Feng, Nat. Mater. **12**, 634 (2013).
[10] J. J. Lee, F. T. Schmitt, R. G. Moore, S. Johnston, Y. T. Cui, W. Li, M. Yi, Z. K. Liu, M. Hashimoto, Y. Zhang, D. H. Lu, T. P. Devereaux, D. H. Lee, and Z. X. Shen, Nature **515**, 245 (2014).
[11] J. F. Ge, Z. L. Liu, C. H. Liu, C. L. Gao, D. Qian, Q. K. Xue, Y. Liu, and J. F. Jia, Nat. Mater. **14**, 285 (2015).
[12] I. I. Mazin, D. J. Singh, M. D. Johannes, and M. H. Du, Phys. Rev. Lett. **101**, 057003 (2008).
[13] P. J. Hirschfeld, M. M. Korshunov, and I. I. Mazin, Rep. Prog. Phys. **74**, 124508 (2011).
[14] C. Fang, Y. L. Wu, R. Thomale, B. A. Bernevig, and J. P Hu, Phys. Rev. X **1**, 011009 (2011).
[15] Y. Zhou, D. H. Xu, F. C. Zhang, and W. Q. Chen, Europhys. Lett. **95**, 17003 (2011).
[16] T. A. Maier, S. Graser, P. J. Hirschfeld, and D. J. Scalapino, Phys. Rev. B **83**, 100515 (2011).
[17] F. Yang, F. Wang, and D. H. Lee, Phys. Rev. B **88**, 100504 (2013).
[18] I. I. Mazin, Phys. Rev. B **84**, 024529 (2011).
[19] Q. Fan, W. H. Zhang, X. Liu, Y. J. Yan, M. Q. Ren, R. Peng, H. C. Xu, B. P. Xie, J. P. Hu, T. Zhang, and D. L. Feng, Nat. Phys. **11**, 946 (2015).
[20] X. F. Lu, N. Z. Wang, H. Wu, Y. P. Wu, D. Zhao, X. Z. Zeng, X. G. Luo, T. Wu, W. Bao, G. H. Zhang, F. Q. Huang, Q. Z. Huang, and X. H. Chen, Nat. Mater. **14**, 325 (2015).
[21] L. Zhao, A. J. Liang, D. N. Yuan, Y. Hu, D. F. Liu, J. W. Huang, S. L. He, B. Shen, Y. Xu, X. Liu, Li Yu, G. D. Liu, H. X. Zhou, Y. L. Huang, X. L. Dong, F. Zhou, Z. X. Zhao, C. T. Chen, Z. Y. Xu, and X. J. Zhou, Nat. Commun. **7**, 10608 (2016).
[22] X. H. Niu, R. Peng, H. C. Xu, Y. J. Yan, J. Jiang, D. F. Xu, T. L. Yu, Q. Song, Z. C. Huang, Y. X. Wang, B. P. Xie, X. F. Lu, N. Z. Wang, X. H. Chen, Z. Sun, and D. L. Feng, Phys. Rev. B **92**, 060504 (2015).
[23] J. E. Hoffman, K. McElroy, D. H. Lee, K. M. Lang, H. Eisaki, S. Uchida, and J. C. Davis, Science **297**, 1148 (2002).
[24] Q. H. Wang and D. H. Lee, Phys. Rev. B **67**, 020511 (2003).
[25] T. Hanaguri, Y. Kohsaka, M. Ono, M. Maltseva, P. Coleman, I. Yamada, M. Azuma, M. Takano, K. Ohishi, and H. Takagi, Science **323**, 923 (2009).
[26] A. V. Balatsky, I. Vekhter, and J. X. Zhu, Rev. Mod. Phys. **78**, 373 (2006).
[27] A. Yazdani, B. A. Jones, C. P. Lutz, M. F. Crommie, and D. M. Eigler, Science **275**, 1767 (1997).
[28] S. H. Pan, E. W. Hudson, K. M. Lang, H. Eisaki, S. Uchida, and J. C. Davis, Nature **403**, 746 (2000).
[29] C. L. Song, Y. L. Wang, P. Cheng, Y. P. Jiang, W. Li, T. Zhang, Z. Li, K. He, L. L. Wang, J. F. Jia, H. H. Hung, C. J. Wu, X. C. Ma, X. Chen, and Q. K. Xue, Science **332**, 1410 (2011).
[30] T. Hanaguri, S. Niitaka, K. Kuroki, and H. Takagi, Science **328**, 474 (2010).
[31] W. Li, H. Ding, P. Deng, K. Chang, C. Song, K. He, L. L. Wang, X. C. Ma, J. P. Hu, X. Chen, and Q. K. Xue, Nat. Phys. **8**, 126 (2012).
[32] H. Yang, Z. Y Wang, D. L. Fang, Q. Deng, Q. H. Wang, Y. Y. Xiang, Y. Yang, and H. H. Wen, Nat. Commun. **4**, 2749 (2013).
[33] See Supplemental Material at http://link.aps.org/supplemental/10.1103/PhysRevB.94.134502 for additional figures and discussions.
[34] N. Hayashi, T. Isoshima, M. Ichioka, and K. Machida, Phys. Rev. Lett. **80**, 2921 (1998).
[35] L. Shan, Y. L. Wang, B. Shen, B. Zeng, Y. Huang, A. Li, D. Wang, H. Yang, C. Ren, Q. H. Wang, S.H. Pan, and H. H. Wen, Nat. Phys. **7**, 325 (2011).
[36] T. Hanaguri, K. Kitagawa, K. Matsubayashi, Y. Mazaki, Y. Uwatoko, and H. Takagi, Phys. Rev. B **85**, 214505 (2012).
[37] D. Huang, C. L. Song, T. A. Webb, S. Fang, C. Z. Chang, J. S. Moodera, E. Kaxiras, and J. E. Hoffman, Phys. Rev. Lett. **115**, 017002 (2015).
[38] Y. Bang, New J. Phys. **16**, 023029 (2014).
[39] X. Chen, S. Maiti, A. Linscheid, and P. J. Hirschfeld, Phys. Rev. B **92**, 224514 (2015).
[40] T. Pereg-Barnea and M. Franz, Phys. Rev. B **78**, 020509(R) (2008).
[41] M. Maltseva and P. Coleman, Phys. Rev. B **80**, 144514 (2009).
[42] P. J. Hirschfeld, D. Altenfeld, I. Eremin, and I. I. Mazin, Phys. Rev. B **92**, 184513 (2015).
[43] P. W. Anderson, J. Phys. Chem. Solids **11**, 26 (1959).
[44] S. Onari and H. Kontani, Phys. Rev. Lett. **103**, 177001 (2009).
[45] D. Zhang, Phys. Rev. Lett. **103**, 186402 (2009).
[46] T. Kariyado and M. Ogata, J. Phys. Soc. Jpn. **79**, 083704 (2010).
[47] S. Grothe, S. Chi, P. Dosanjh, R. X. Liang, W. N. Hardy, S. A. Burke, D. A. Bonn, and Y. Pennec, Phys. Rev. B **86**, 174503 (2012).
[48] J. X. Zhu, R. Yu, A. V. Balatsky, and Q. M. Si, Phys. Rev. Lett. **107**, 167002 (2011).
[49] Q. E. Wang, Z. J. Yao, and F. C. Zhang, Europhys. Lett. **101**, 57002 (2013).
[50] S. Mukherjee, M. N. Gastiasoro, and B. M. Andersen, Phys. Rev. B **88**, 134508 (2013).
[51] R. Beaird, I. Vekhter, and J. X. Zhu, Phys. Rev. B **86**, 140507(R) (2012).
[52] X. Chen, V. Mishra, S. Maiti, and P. J. Hirschfeld, Phys. Rev. B **94**, 054524 (2016).
[53] H. Kontani and S. Onari, Phys. Rev. Lett. **104**, 157001 (2010).
[54] Z. Y. Du, X. Yang, H. Lin, D. L. Fang, G. Du, J. Xing, H. Yang, X. Y. Zhu, and H. H. Wen, Nat. Commun. **7**, 10565 (2016).